J Mater Sci (2009) 44:2743–2751
DOI 10.1007/s10853-009-3358-2

Single step synthesis of nanosized CeO_2–M_xO_y mixed oxides (M_xO_y = SiO_2, TiO_2, ZrO_2, and Al_2O_3) by microwave induced solution combustion synthesis: characterization and CO oxidation

Benjaram M. Reddy · Gunugunuri K. Reddy · Ibram Ganesh · Jose M. F. Ferreira

Received: 22 December 2008 / Accepted: 17 February 2009 / Published online: 9 March 2009

Abstract Various CeO_2–M_xO_y ($M_xO_y = SiO_2$, TiO_2, ZrO_2, and Al_2O_3) mixed oxides were prepared by microwave induced solution combustion method and analyzed by different complimentary techniques, namely, X-ray diffraction (XRD), Raman spectroscopic (RS), UV–Vis diffuse reflectance spectroscopy (UV-DRS), X-ray photoelectron spectroscopy (XPS), thermogravimetry (TG-DTA), and BET surface area. XRD analyses revealed that CeO_2–SiO_2 and CeO_2–TiO_2 mixed oxides are in slightly amorphous form and exhibit only broad diffraction lines due to cubic fluorite structure of ceria. XRD lines due to the formation of cubic $Ce_{0.5}Zr_{0.5}O_2$ were observed in the case of CeO_2–ZrO_2 sample. RS results suggested defective structure of the mixed oxides resulting in the formation of oxygen vacancies. The UV-DRS measurements provided valid information about $Ce^{4+} \leftarrow O^{2-}$ and $Ce^{3+} \leftarrow O^{2-}$ charge transfer transitions. XPS studies revealed the presence of cerium in both Ce^{3+} and Ce^{4+} oxidation states. The ceria–zirconia combination exhibited better oxygen storage capacity (OSC) and CO oxidation activity when compared to other samples. The significance of present synthesis method lays mostly on its simplicity, flexibility, and the easy control of different experimental factors.

Introduction

Combustion synthesis has emerged as an effective method for the preparation of homogeneous, finely dispersed crystalline uni- and multicomponent oxides [1–8], as well as metals and alloys of uniform composition and size [9, 10]. This method is quick and straightforward without the involvement of time consuming intermediate preparative steps. Some other advantages of combustion synthesis are the use of relatively simple equipment, the formation of high purity products, the stabilization of metastable phases, and the formation of virtually any size and shape products. The solution combustion method is an alternative approach to self-propagating high temperature synthesis in producing homogeneous products with low ignition temperatures [3]. In solution combustion synthesis, organic compounds containing reducible functional groups are employed as fuels and metal nitrates as oxidizers. The exothermic redox reaction between the fuel and the oxidizer results in the formation of unagglomerated solid particles with simultaneous evolution of large amount of gaseous products [8, 11–14]. The initiation of the exothermic redox reaction by a heating source is very important because it needs rapid and efficient heating. Of course, in recent times conventional heating techniques have been substituted by microwave dielectric heating. Microwave is an attractive heating tool for solid state synthesis owing to an increase in the synthesis rate, and for the peculiar property of the microwaves to heat the system 'from the inside' [15]. However, the exact nature of microwave interactions with reactants during the synthesis of materials is somewhat unclear and speculative.

Ceria is a candidate material for various applications in different fields including fuel-cell processes [16, 17], oxygen permeation membrane systems [18–20], and as

B. M. Reddy (✉) · G. K. Reddy
Inorganic and Physical Chemistry Division, Indian Institute of Chemical Technology, Hyderabad 500607, India
e-mail: bmreddy@iict.res.in

I. Ganesh
International Advanced Research Centre for Powder Metallurgy and New Materials (ARCI), Balapur (PO), Hyderabad 500005, India

J. M. F. Ferreira
Department of Ceramics and Glass Engineering, CICECO, University of Aveiro, Aveiro 3810193, Portugal

catalysts in numerous economically and technologically important industrial processes. Their use in the domain of catalysis is on the basis of superior chemical and physical stability, high oxygen mobility, and high oxygen vacancy concentration, which are characteristic of the fluorite-type oxides. The facile cycling between reduced and oxidized states ($Ce^{3+} \leftrightarrow Ce^{4+}$) permits the reversible addition and removal of O_2 from the CeO_2 [21–23]. All these features explain the applicability of these materials as promoters in fluid catalytic cracking processes (FCC) or as an active component of three-way catalysts (TWC) for environmental protection purposes [21–23]. Also their use in several other emerging catalytic processes include total oxidation of different hydrocarbons [21, 23], wet oxidation of organic compounds [19, 22], the removal of total organic carbon from industrial wastewaters [24], water–gas shift reaction [25, 26], methane reforming with CO_2 [27, 28], SO_2 reduction with CO [29], and finally in deNO$_x$ catalysis [30].

The catalytic efficiency of ceria is normally suppressed at elevated temperatures because of sintering and loss of surface area; sintering also causes a loss of oxygen storage capacity. Besides that, the preparation of ceria-containing materials with sufficiently high specific surface area at higher temperatures is still not an established technology. Ceria stabilized with alumina or silica has been found to be an efficient catalyst, especially for environmental applications such as combustion or removal of pollutants from auto-exhaust streams [21, 23]. On those lines special attention has been focused on the preparation of ceria–zirconia and ceria–titania solid solutions [22, 23]. So far several preparative routes have been proposed in the literature for the synthesis of ceria-based materials. The reports on the synthesis of ceria-based mixed oxides by combustion synthesis using microwave dielectric heating are very rare. In this article, we report on the microwave induced solution combustion synthesis of CeO_2–M_xO_y ($M_xO_y = SiO_2$, Al_2O_3, ZrO_2, and TiO_2) mixed oxides. These structured catalysts are prepared rapidly, without aging and calcination steps, in a ready-to-use form. The physicochemical characteristics of these materials were investigated by various techniques, namely, XRD, Raman, UV-DRS, XPS, and other techniques, and the catalytic properties were evaluated for oxygen storage capacity and CO oxidation measurements.

Materials and methods

Preparation of materials

To synthesize various CeO_2–M_xO_y ($M_xO_y = SiO_2$, Al_2O_3, ZrO_2, and TiO_2) mixed oxides by microwave induced solution combustion synthesis method, the corresponding nitrates were chosen as precursors, since nitrates favor combustion. The nitrate precursors of silicon and titanium are not available. Initially their respective metal alkoxides were converted into their corresponding metal nitrates (oxidizers) and then reacted with urea to produce the mixed oxide powders and the reactions can be expressed as follows:

$$Ti(i{-}OC_3H_7)_4 + 3H_2O \rightarrow TiO(OH)_2 + 4C_3H_7OH$$
$$TiO(OH)_2 + 2HNO_3 \rightarrow TiO(NO_3)_2 + 2H_2O$$
$$Si(OC_2H_5)_4 + 3H_2O \rightarrow SiO(OH)_2 + 4C_2H_5OH$$
$$SiO(OH)_2 + 2HNO_3 \rightarrow SiO(NO_3)_2 + 2H_2O$$

To prepare ceria–alumina mixed oxides, the requisite quantities of cerium(III) nitrate (Aldrich, AR grade) and aluminum(III) nitrate (Fluka, AR grade) were dissolved separately in deionized water and mixed together in a Pyrex glass dish ($\phi = 150 \times 80$ mm^2). A stoichiometric quantity (as per the concept used in propellant chemistry) of solid urea (Fluka, AR grade) was added to the aforementioned mixture solution and stirred rigorously to obtain a clear solution. The dish containing the reaction mixture was introduced into a modified domestic microwave oven (BPL, India Limited, BMO-700T, 2.54 GHz, 700 W). Initially, the solution boils and undergoes dehydration followed by decomposition and spontaneous combustion with the evolution of large amounts of gases, including N_2, CO_2, and H_2O along with some small traces of NH_3 and NO_2, followed by a spontaneous flame resulting in a light yellow residual mass. The entire process in the microwave oven from dehydration to combustion took around 40 min. Three to four experiments were conducted under identical conditions to check for reproducibility. Properties of all the synthesized powders were found to be identical. Other mixed oxides were also prepared in the same manner from their corresponding nitrates.

Characterization techniques

The TGA/DTA curves were obtained on a Mettler Toledo TG-SDTA apparatus. The sample with ca. 12 mg was heated from ambient temperature to 1173 K under a nitrogen flow at the heating rate of 10 K/min. The BET surface areas were determined by N_2 adsorption, using a SMART instrument. Prior to analysis, the samples were oven-dried at 423 K for 12 h and flushed with argon gas for 2 h. XRD patterns were recorded on a Rigaku Miniflex diffractometer, using Ni-filtered Cu Kα (0.15418 nm) radiation source. The intensity data were collected over a 2θ range of 3° to 80°, with a 0.02° step size and using a counting time of 1s per point. Crystalline phases were identified by comparison with the reference data from International Centre for Diffraction Data (ICDD) files. The average crystallite size of CeO_2 was estimated with the help of the Debye-Scherrer equation, using the XRD data of all prominent lines [31]. The diffuse reflectance spectra were obtained over the wavelength range 200–800 nm using a GBS-Cintra 10e UV–Vis NIR spectrophotometer with integration sphere diffuse reflectance attachment. Samples were diluted in a KBr matrix and palletized. The obtained spectra were processed with SPECTRAL 1.70 software, consisting of calculation of $F(R_\infty)$ from the absorbance. The Raman spectra were recorded on a triple subtractive HORIBA JOBIN YVON HR 800 Raman spectrometer at ambient temperature. The emission line at 632.81 nm from the Ar^+ ion laser was focused. The power of the incident beam on the sample was about 3 mW. Time of acquisition was adjusted according to the intensity of the Raman scattering. The wavenumber values reported from the spectra are accurate to within 2 cm^{-1}. For each solid, the spectra were recorded at several points of the sample (more than six), to ascertain the homogeneity of the sample, and the average of all these spectra were plotted in the figure presented in this study. The XPS measurements were performed on a KRATOS AXIS 165 spectrometer using Mg Kα (1253.6 eV) radiation as the excitation source. Charging of the catalyst samples was corrected by setting the binding energy of the adventitious carbon (C 1s) at 284.6 eV [32, 33]. The XPS analysis was performed at ambient temperature and at pressures typically on the order of 10^{-10} Pa. Prior to analysis, the samples were out gassed in a vacuum oven overnight.

Activity measurements

The potential OSC was examined by oxygen release characteristics of the powders in the temperature range 573–1073 K. The change in the weight of the sample was monitored by thermogravimetry (TG) under cyclic heat treatments in flowing nitrogen and dry air. A commercial Mettler Toledo TG-DTA analyzer was employed for this purpose. The heat cycle consisted of heating the sample to 1073 K in N_2, cooling down to 423 K in dry air, and again heating to 1073 K in N_2 environment. All heating and cooling rates were 5 K min^{-1}. The weight loss of sample during the second heating cycle was used to measure the oxygen release properties. CO oxidation was conducted in a fixed-bed micro-reactor under normal atmospheric pressure at 300–773 K using a heating ramp of 5 K min^{-1}. About 100 mg catalyst sample (250–355 μm sieve fraction) diluted with quartz particles of the same sieve fraction was placed in a quartz reactor for evaluation. Temperature was measured directly at the catalyst bed, using a thermocouple placed in the reactor. The following gases and gas mixtures were used (supplied by Air Liquide): argon (>99.999% purity), 9.98% CO in argon (CO purity, >99.997%; argon purity, >99.99%), and 10.2% O_2 in argon (oxygen purity, >99.995%). The total flow rates maintained by three mass flow controllers were in the range of 50–100 N mL min^{-1} (milliliters normalized to 273.15 K and 1 atmosphere). The CO and CO_2 gas concentrations were measured using an Uras 14 infrared analyzer module, and the O_2 concentration was measured using a Magnos 16 analyzer (Hartmann & Braun). Prior to oxidation of CO, the catalysts were heated to 773 K in 10.2% O_2/Ar gas mixture, using a heating ramp of 10 K min^{-1}, and kept at the final temperature for 1 h. The oxidized sample was then purged in argon and cooled to the desired starting temperature. The CO/O_2 reactant feed ratio was 1, and partial pressures of CO and O_2 were in the range of 10 mbar.

Results and discussion

Synthesis of materials and reaction stoichiometry

The combustion of metal nitrates–urea mixture occurred as a self-propagating and non-explosive exothermic reaction. Initially urea burns and decomposes into carbon dioxide and water giving rise to a large amount of gases and reaching temperatures in excess of 1273 K. The redox reaction can be written as follows:

$$CO(NH_2)_2 + 1.5O_2 \rightarrow CO_2(g) + 2H_2O(g) + N_2(g)$$

This reaction is exothermic [-129.9 kcal (ΔH_f^0, 298 K)] and supplies the required heat for the completion of the powder synthesis reaction.

Besides urea, various other fuels [34, 35] have been used in the combustion synthesis of a variety of single and mixed oxides, all of them containing nitrogen but differing in ‘reducing power’ and the amount of gases they generate, which obviously affects the characteristics of the reaction products. The reaction is not isothermal and larger amounts of gases dissipate more heat, thereby, preventing the oxides from sintering, since the temperature reached is not so high. The coincident sintering effect in the higher temperature reactions may result in a loss of sub-micron features of the powders. Urea has the lowest reducing power (total valencies 16) and produces the smallest volume of gas (4 mol mol^{-1} of urea). Also it is readily available commercially, cheap and generates the highest temperature, although fuel-rich mixtures might produce prematurely sintered particle agglomerates [36].

As oxidizers, metal nitrates are the preferred salts because they also contain nitrogen, water soluble (a good homogenization can be achieved in the solution) and a few hundred degrees are usually enough to melt them. Hydrate salts are even more favored in this respect, although the water molecules do not affect the total valencies of the nitrate and are, therefore, irrelevant for the chemistry of the combustion.

The powder characteristics like crystallite size, surface area, and nature of agglomeration are primarily governed by enthalpy or flame temperature generated during combustion, which itself is dependent on the nature of fuel and fuel to oxidant ratio. According to the concepts of propellant chemistry, for a stoichiometric redox reaction between a fuel and an oxidizer, the ratio of the net oxidizing valency of the metal nitrates to the net reducing valency of the fuel should be unity [37, 38]. Chick et al. [39] showed that in the case of glycine-nitrate combustion, primarily N_2, CO_2, and H_2O are evolved as the gaseous products. Therefore, carbon and nitrogen were considered as reducing elements with the corresponding valencies 4+ and 1+, while oxygen is considered as an oxidizing element with the valency 2−. Metals are also considered as reducing elements and the valencies of Ce, Zr, Ti, Si are 3+, 4+, 4+, 4+, respectively [37, 38]. From the total oxidizing and reducing valencies of metal nitrates and urea, the amount of urea required for the preparation of CeO_2–SiO_2 mixed oxide can be calculated as follows: The total oxidizing and reducing valencies of $Ce(NO_3)_3$, $SiO(NO_3)_2$, and urea are −15, −10, and +6. The amount of urea required in this process can be estimated by balancing the following equation

$$\begin{aligned}
&1\left(\mathrm{Ce(NO_3)_3}\right) + 1\left(\mathrm{SiO(NO_3)_2}\right) + x(\mathrm{NH_2CONH_2}) = 0\\
&1(-15) + 1(-10) + x(6) = 0\\
&x = 4.66 \text{ moles}
\end{aligned}$$

Assuming complete combustion, the theoretical equation for the redox reaction between metal nitrates and urea can be expressed as follows:

$$\begin{aligned}
&\mathrm{Ce(NO_3)_3 + SiO(NO_3)_2 + 4.66NH_2CONH_2 + O_2}\\
&\rightarrow \mathrm{CeO_2{-}SiO_2 + 7.16N_2\uparrow + 4.66CO_2\uparrow + 9.32H_2O\uparrow}
\end{aligned}$$

Similarly, for the preparation of CeO_2–Al_2O_3, CeO_2–ZrO_2, and CeO_2–TiO_2 mixed oxides the amount of urea required is 5.00, 4.66, and 4.66 moles, respectively. By assuming complete combustion the theoretical equations for the formation of CeO_2–Al_2O_3, CeO_2–ZrO_2, and CeO_2–TiO_2 mixed oxides can be written as follows:

$$\begin{aligned}
&\mathrm{Ce(NO_3)_3 + Al(NO_3)_3 + 5NH_2CONH_2 + O_2}\\
&\rightarrow \mathrm{CeO_2{-}Al_2O_3 + 8N_2\uparrow + 5CO_2\uparrow + 10H_2O\uparrow}\\
&\mathrm{Ce(NO_3)_3 + ZrO(NO_3)_2 + 4.66NH_2CONH_2 + O_2}\\
&\rightarrow \mathrm{CeO_2{-}ZrO_2 + 7.16N_2\uparrow + 4.66CO_2\uparrow + 9.32H_2O\uparrow}\\
&\mathrm{Ce(NO_3)_3 + TiO(NO_3)_2 + 4.66NH_2CONH_2 + O_2}\\
&\rightarrow \mathrm{CeO_2{-}TiO_2 + 7.16N_2\uparrow + 4.66CO_2\uparrow + 9.32H_2O\uparrow}
\end{aligned}$$

Characterization of product mixed oxides

The synthesized CeO_2–M_xO_y (M_xO_y = SiO_2, Al_2O_3, ZrO_2, and TiO_2) mixed oxides were subjected to TG analysis in the range of 323–1273 K. The obtained thermograms (not shown) revealed one major and one minor weight loss peaks. In all cases, the first major weight loss peak in the region 323–473 K was due to loss of adsorbed water on the surface of the sample. The second minor weight loss peak in the region 573–723 K could be attributed to decomposition of unreacted nitrates and urea [40]. The weight loss in this region was about ~1% for all the mixed oxides, suggesting that almost all the nitrates were decomposed into oxides and complete combustion was achieved. The weight loss beyond 723 K was about 0.5% for all samples, indicating that over the temperature range of 723–1273 K, the mixed oxides are quite stable in terms of chemical composition. The N_2 BET surface areas of various samples prepared in this study are presented in Table 1. All the samples exhibit reasonably high specific surface areas. As expected, ceria–silica sample exhibited high surface area compared to other samples. This may be due to the use of alkoxide precursor as well as dispersion of smaller ceria particles over the surface of silica. The decreasing order of surface areas is as follows: CeO_2–SiO_2 > CeO_2–TiO_2 > CeO_2–ZrO_2 > CeO_2–Al_2O_3. Interestingly, samples prepared from the alkoxide precursors exhibited higher surface areas compared to the samples obtained from direct nitrate precursors.

The X-ray powder diffraction patterns of various samples prepared in the present study are shown in Fig. 1. As can be noted from this figure, the ceria–silica mixed oxide exhibits amorphous nature. It is difficult to resolve the peaks. Ceria–titania mixed oxide exhibited poor crystallinity and only broad diffraction lines due to cubic fluorite structure of ceria (PDF-ICDD 34-0394) could be seen. There are no peaks corresponding to either TiO_2 or compounds between ceria and titania. In our earlier investigation, formation of titania-anatase phase was observed in ceria–titania mixed oxides prepared by a conventional co-precipitation method [41]. Preuss and Gruehn [42] reported various Ce–Ti-oxides namely, Ce_2TiO_5, $Ce_2Ti_2O_7$, and $Ce_4Ti_9O_{24}$ by heating the appropriate mixtures of solids containing Ce and Ti at 1523 K. Hegde and coworkers [43]

Table 1 BET surface area, crystallite size, and oxygen storage capacity values of various ceria based mixed oxides (MWCS: CeO_2–SiO_2, MWCZ: CeO_2–ZrO_2, MWCT: CeO_2–TiO_2, MWCA: CeO_2–Al_2O_3)

Sample	BET surface area (m^2/g)	Crystallite size (nm)	OSC μ moles O_2/g of CeO_2
MWCS	125	nd	126
MWCZ	56	12.5	278
MWCT	79	9.6	211
MWCA	38	17.5	186

nd not determined due to amorphous nature

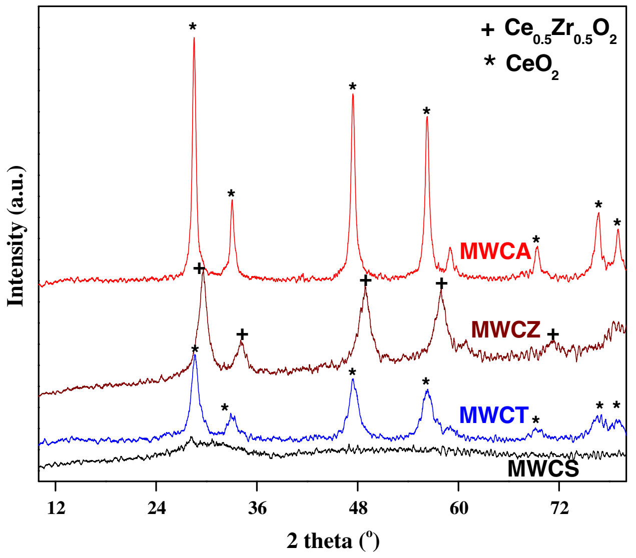

Fig. 1 X-ray diffraction patterns of various CeO_2–M_2O_3 mixed oxides (MWCS: CeO_2–SiO_2, MWCZ: CeO_2–ZrO_2, MWCT: CeO_2–TiO_2, MWCA: CeO_2–Al_2O_3)

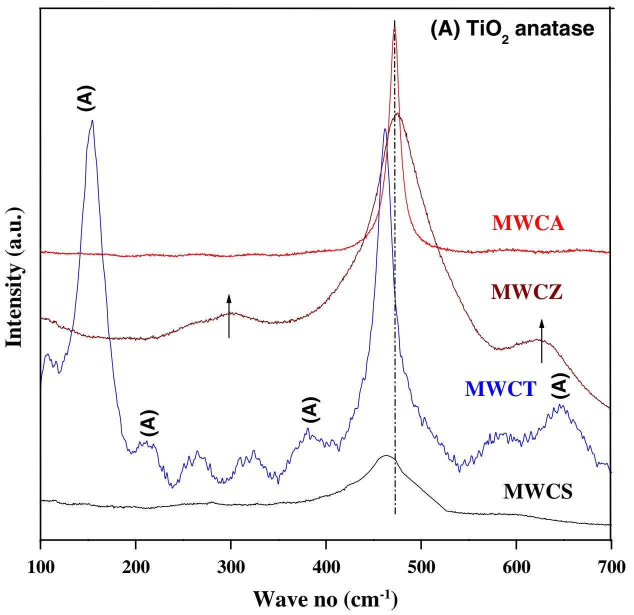

Fig. 2 Raman spectra of various CeO_2–M_2O_3 mixed oxides (MWCS: CeO_2–SiO_2, MWCZ: CeO_2–ZrO_2, MWCT: CeO_2–TiO_2, MWCA: CeO_2–Al_2O_3)

reported formation of various solid solutions between ceria and titania prepared by sol–gel method. The absence of compounds or solid solutions may be due to a different preparation method adopted in the present investigation. Formation of a solid solution of specific composition $Ce_{0.5}Zr_{0.5}O_2$ (PDF-ICDD 34-1436) was observed in case of ceria–zirconia mixed oxide. This is primarily due to incorporation of Zr^{4+} cations into the cubic fluorite structure of ceria as reported by several authors [44, 45]. As can be noted from Fig. 1, the ceria–alumina mixed oxide exhibits better crystallinity compared to other mixed oxides. Crystallite sizes of CeO_2 in CeO_2–SiO_2, CeO_2–TiO_2 and CeO_2–Al_2O_3, and $Ce_{0.5}Zr_{0.5}O_2$ in CeO_2–ZrO_2 are summarized in Table 1. As can be noted from Table 1, the crystallite size depends on the type of additive oxide incorporated and the nature of precursor used. The crystallite sizes of all mixed oxides are in nanometer range. In particular, the crystallite size of ceria in ceria–silica mixed oxide is relatively small compared to other samples. This may be due to stabilization of smaller ceria particles in the silica matrix.

Raman spectra of various samples prepared in the present study are shown in Fig. 2. In general, the Raman spectrum of CeO_2 is characterized by a strong band at 462 cm^{-1} which is due to the F_{2g} Raman active mode of the fluorite structure [46]. In addition, it exhibits a weak band at ~260 cm^{-1} and a shoulder at ~600 cm^{-1}, which have been attributed, respectively, to the normal Raman inactive (IR active) transverse and longitudinal optical phonon modes at the Brillouin zone center [47]. As shown in Fig. 2, Raman spectra of CeO_2–SiO_2 mixed oxide is broad and exhibits a peak at ~464 cm^{-1}. The band at ~464 cm^{-1} corresponds to the triply degenerate F_{2g} mode and can be viewed as a symmetric breathing mode of the O atoms around Ce ions [48]. The broadness of the spectrum may be due to smaller crystallite size of the ceria as evidenced by XRD results [49]. It is known that the intensity of Raman band is dependent on several factors, including the grain size and morphology. In general, inhomogeneous strain and phonon confinement are responsible for the broad and asymmetric character of the bands as the particle size gets smaller [50]. In addition to the band at 464 cm^{-1}, a weak band was observed at 600 cm^{-1}. This could be attributed to non-degenerate longitudinal optical mode of CeO_2 [48, 51]. Normally, this mode should not be observed by RS; however, the presence of some defects can involve relaxation of the selection rules. In particular, this band has been linked to oxygen vacancies in the CeO_2 lattice [52]. SiO_2 did not show any Raman features, as reported in the literature [53]. As presented in Fig. 2, the Raman spectra of ceria–titania shows a typical spectra of TiO_2 (anatase) (space group *I*41/*amd*) and CeO_2. The Raman bands pertaining to the TiO_2 (anatase) phase appear at 155, 211, 380, and 645 cm^{-1}, whereas CeO_2 exhibits peaks at 272, 460, and 570 cm^{-1}, which are in agreement with the literature reports [46]. The Raman spectrum of CeO_2–ZrO_2 also shows a strong band at ~470 cm^{-1} and a less-prominent broad band at ~600 cm^{-1}. In addition to these two bands, a weak band was observed at 305 cm^{-1}, which could be attributed to displacement of oxygen atoms from their ideal fluorite lattice positions. No Raman lines pertaining to ZrO_2 could be observed, which is inline with the XRD measurements. According to the literature, six Raman active modes ($A_{1g} + 3E_g + 2B_{1g}$) are expected for *t*-ZrO_2 (space group *P*42/*nmc*), whereas, for the cubic fluorite structure of CeO_2 (space group *Fm*3*m*), only one mode is Raman active [54]. The Raman spectra of ceria–alumina are quite intense compared to other samples and exhibit only a prominent peak at 464 cm^{-1}. This could be attributed to the F_{2g} vibration of the fluorite-type lattice.

DRS has been used extensively to study ceria-based materials and transition metal oxides to obtain information on surface coordination and different oxidation states of the metal ions by measuring d–d, f–d transitions and oxygen–metal ion charge transfer bands. However, this technique has limitations due to the difficulty in interpreting large bandwidths and specular reflectance often observed in the spectra [55]. Various synthesized samples were investigated by DRS technique and the spectra are presented in Fig. 3. The spectra, in general, are broad and exhibited a myriad of poorly resolved peaks. All samples exhibit three absorption maxima centered at ~255, 285, and 340 nm. The latter two absorption maxima are ascribed to $Ce^{4+} \leftarrow O^{2-}$ charge transfer and interband transitions, respectively. The former maxima correspond to $Ce^{3+} \leftarrow O^{2-}$ charge transfer transitions [56]. In case of ceria–zirconia sample, the absorption edge was slightly shifted. Substitution of Zr^{4+} cations into the ceria lattice leads to lowering of symmetry and consequent strain development at the cerium sites. This may be the cause for the observed shift [57]. The band at ~255 nm, which has been characterized as $Ce^{3+} \leftarrow O^{2-}$ charge transfer transition, is more intense in ceria–zirconia mixed oxide compared to other samples with a slight blue-shift toward lower wavelength. The occurrence of oxygen vacancy defects, as noticed from RS studies, support the $Ce^{3+} \leftarrow O^{2-}$ transitions, which is more intense in the ceria–zirconia sample.

Photoelectron spectroscopy was used to obtain further information about the valence/oxidation state of the elements and surface composition of the mixed oxides by inspecting the spectral line shape and the signal intensities associated with the core-level electrons. The CeO_2 3d photoelectron peaks of various samples investigated in the present study are shown in Fig. 4. The electron binding energies of O 1s, Si 2p, Ti 2p, Zr 3d, Al 2p, and Ce 3d photoelectron peaks are presented in Table 2. As shown in Fig. 4, the Ce 3d spectra consists of two sets of spin-orbit multiplets featuring $3d_{3/2}$ and $3d_{5/2}$ (represented as u and v, respectively) contributions [58]. The peaks v (~883 eV) and u (~902 eV) are the main lines corresponding to Ce^{4+} state, whereas features represented as v″, v‴, u″, and u‴ are the satellites related to this state. The main signals of Ce^{3+} (v_0, u_0) are generally noticed at around 881 and 898 eV, respectively. The latter peak is normally observed overlapping with v‴. The satellites to these features are represented by v′and u′, respectively, which indicate the presence of Ce^{3+}. Presence of Ce^{4+} state is normally supported by the intensity of u‴ peak. Thus, on the surface of the samples, concentration of both Ce^{4+} and Ce^{3+} are normally accounted based on the intensities of these features [59–61]. The observed binding energy values of all the components involved are in good agreement with the literature reports [62]. The spectra pertaining to ceria–silica mixed oxide is too broad and it was very difficult to

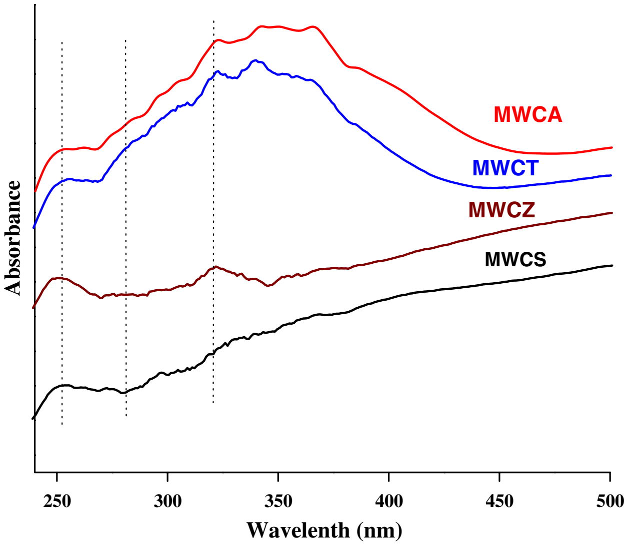

Fig. 3 UV-DRS spectra of various CeO_2–M_2O_3 mixed oxides (MWCS: CeO_2–SiO_2, MWCZ: CeO_2–ZrO_2, MWCT: CeO_2–TiO_2, MWCA: CeO_2–Al_2O_3)

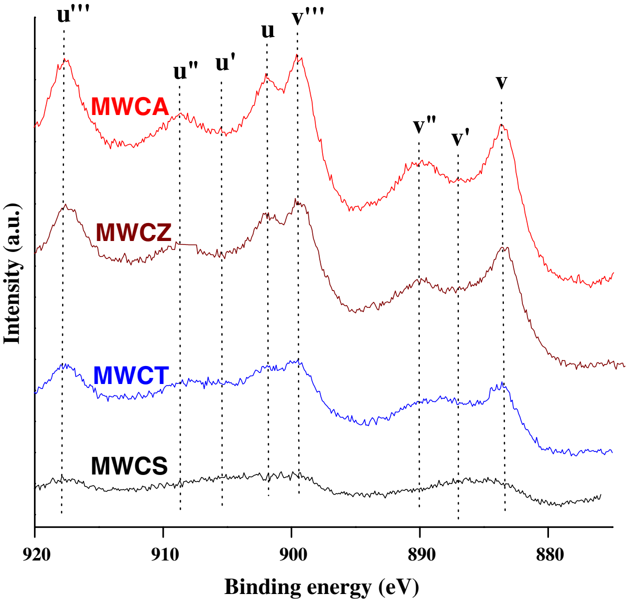

Fig. 4 Ce 3d XPS spectra of various CeO_2–M_2O_3 mixed oxides (MWCS: CeO_2–SiO_2, MWCZ: CeO_2–ZrO_2, MWCT: CeO_2–TiO_2, MWCA: CeO_2–Al_2O_3)

Table 2 XPS binding energies (eV) of various ceria based mixed oxides (MWCS: CeO_2–SiO_2, MWCZ: CeO_2–ZrO_2, MWCT: CeO_2–TiO_2, MWCA: CeO_2–Al_2O_3)

Sample	Ce 3d	O 1s	Si 2p	Ti 2p	Zr 3d	Al 2p
MWCS	883.3	529.3–533	102.9	–	–	–
MWCT	883.4	530.1	–	458.7	–	–
MWCZ	883.1	530.5	–	–	182.3	–
MWCA	883.4	530.3	–	–	–	73.8

identify the peaks. Very complicated and broad spectra were observed for ceria–titania comprising the peaks pertaining to Ce^{4+} and Ce^{3+} oxidation states. The spectra pertaining to ceria–zirconia sample also indicate the presence of both Ce^{3+} and Ce^{4+} oxidation states, in accordance with literature reports that Ce becomes easily reducible due to formation of solid solutions with zirconia and such reduction was found to be maximum for the composition $Ce_{0.5}Zr_{0.5}O_2$ [63]. The ceria–alumina mixed oxide exhibits quite intense peaks compared to other samples and also shows the peaks corresponding to Ce^{3+} and Ce^{4+} oxidation states. As can be noticed from Fig. 4, the Ce^{3+} and Ce^{4+} distribution is highly dependent on the nature of the additive oxide incorporated into the ceria lattice.

Figure 5 displays the O 1s XP spectra of various samples investigated in this study. The O 1s peak is generally broad and complicated, because of the nonequivalence of surface O ions. As per the literature, the O ions in pure CeO_2 exhibit intense peaks at 528.6, 528.8, 529.6, and 530.1 eV, respectively. The O 1s binding energy values reported for various other oxides namely, SiO_2, TiO_2, ZrO_2, and Al_2O_3 are 532.7, 530.0, 530.6 eV, and 531.4, respectively [49, 64–66]. As can be noted from Fig. 5, the ceria–silica mixed oxide exhibits a broad peak in the region of 529.3–532.9 eV. The broadness may be due to smaller crystallites and presence of different oxide components. The O 1s spectra (Fig. 5) obtained for other mixed oxides are fairly similar, and show a peak at 530.1 eV and a small additional peak at 532.5 eV. The peak at about 530.1 eV is due to the ionization of oxygen associated with various mixed oxides, while the small peak at about 532.6 eV may be attributed to the adsorbed oxygen (possibly from absorbed water and/or carbonates) [67]. The binding energy values of Si 2p, Zr 3d, Ti 2p, and Al 2p presented in Table 2 are in good agreement with the literature reports [41, 64, 67–69].

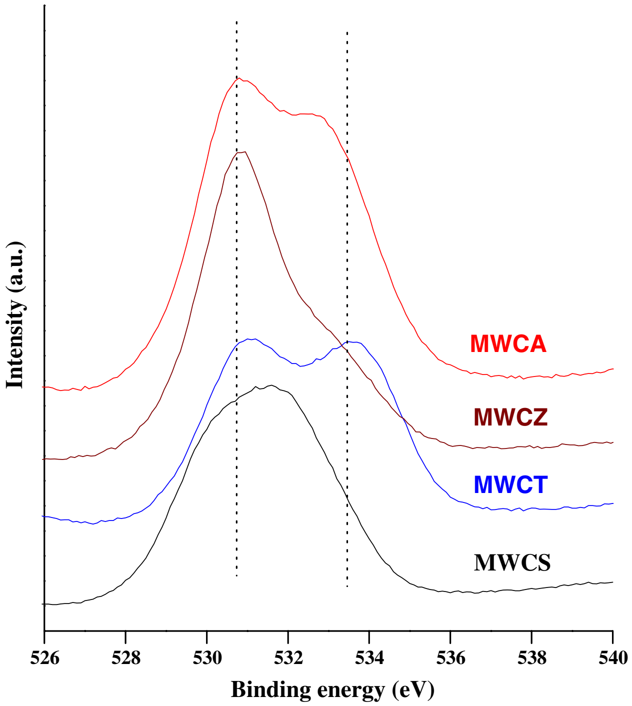

Fig. 5 O 1s XPS spectra of various CeO_2–M_2O_3 mixed oxides (MWCS: CeO_2–SiO_2, MWCZ: CeO_2–ZrO_2, MWCT: CeO_2–TiO_2, MWCA: CeO_2–Al_2O_3)

A TG method under cyclic heat treatments in flowing air in the temperature range of 573–1073 K was used to measure the OSC property of the synthesized mixed oxides [42, 70]. The total OSC values of various samples presented in Table 1 show the following decreasing order: CeO_2–ZrO_2 > CeO_2–TiO_2 > CeO_2–Al_2O_3 > CeO_2–SiO_2. The total OSC of ceria and the factors that affect the OSC, such as surface area, particle size, method of preparation, and nature of foreign oxide are still not completely understood. However, it is clear from the analysis of these parameters that the OSC is not substantially improved by small particle size or high specific surface area. Though ceria–silica bears highest specific surface area and smallest crystallite size among the investigated samples, the OSC value is lowest for this sample. A predominant increase in the OSC of CeO_2–ZrO_2 when compared to other systems could be noted from Table 1. From a structural point of view, there is a quite significant misfit between the ionic radii of Ce^{4+} (0.97 Å) and Zr^{4+} (0.84 Å), which is responsible for modification of the CeO_2 lattice upon insertion of ZrO_2. The intense Raman band observed at 600 cm^{-1} supports the OSC results. Distortion of O_2-sub lattice in the mixed oxide permits a higher mobility of the lattice oxygen, and reduction is no longer confined to the surface but extends deep into the bulk. This gives an impression that the bulk oxygen diffusion rate must be sufficiently large and the observed OSC is controlled by thermodynamic equilibrium of the redox reaction.

Catalytic activity for CO oxidation

The catalytic activity of various mixed oxides was tested for CO oxidation. The activity measurements were performed at normal atmospheric pressure and the conversion

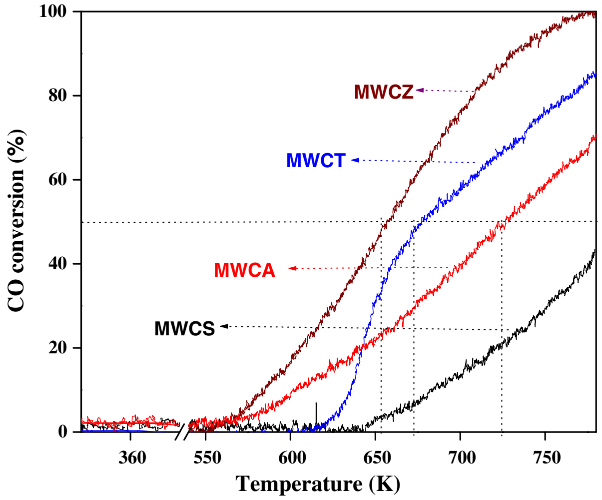

Fig. 6 Conversion of CO versus temperature profiles of various CeO_2–M_2O_3 mixed oxides (MWCS: CeO_2–SiO_2, MWCZ: CeO_2–ZrO_2, MWCT: CeO_2–TiO_2, MWCA: CeO_2–Al_2O_3)

of CO was evaluated as per earlier reports [71, 72]. The conversion of CO as a function of reaction temperature is presented in Fig. 6, which corroborates well with the OSC measurements. As expected, CeO_2–ZrO_2 sample exhibited better performance than the other samples. Among all the samples, ceria–zirconia sample exhibited highest conversion (100%) followed by ceria–titania (85%), ceria–alumina (70%), and ceria–silica (40%), respectively, at the highest temperature investigated in the present study. The light off temperatures for ceria–zirconia, ceria–titania, and ceria–alumina samples are 654, 677, and 727 K, respectively. In our earlier investigation [45] also we observed that silica supported ceria–zirconia mixed oxide exhibits lesser CO oxidation activity compared to alumina and titania supported samples, although it possessed higher surface area and smaller crystallite size. Therefore, the present results corroborate well with the literature reports. It is generally accepted that CO oxidation under stationary conditions occurs over pure ceria by a Mars–van Krevelen-type mechanism, where reaction involves alternate reduction and oxidation of the ceria surface with the formation of surface oxygen vacancies (as the key step) and their successive replenishment by gas-phase oxygen [71, 73]. During the course of catalytic CO oxidation, one has to activate either of the reactants and this occurs preferentially with oxygen. Thus, in catalytic CO oxidation molecular oxygen is generally dissociated into radicals, which are strong oxidizers, as well as strong electrophiles. From these observations, it may be concluded that the higher the OSC of the catalyst, the higher the activity for CO oxidation. More than the total OSC, the local concentration of sites for O_2 adsorption would be a determining factor in CO oxidation. A close correlation between OSC and catalytic activity may, however, be found since a high concentration in anionic vacancy is a prerequisite for a high OSC value of the sample.

Summary

By adopting a simple single step microwave induced solution combustion synthesis method various CeO_2–M_xO_y ($M_xO_y = SiO_2$, TiO_2, ZrO_2, and Al_2O_3) mixed oxides with sufficiently higher surface areas were prepared. TGA results revealed that all the nitrates were decomposed into oxides and complete combustion was achieved in all cases. XRD results revealed that ceria–silica and ceria–titania mixed oxides were in slightly amorphous form and ceria–alumina mixed oxide was in crystalline form. A specific solid solution $Ce_{0.5}Zr_{0.5}O_2$ was formed in case of ceria–zirconia mixed oxide. The UV-DRS results enable to conclude that some amount of Ce^{3+} was present in all the mixed oxides. Raman measurements established the fluorite structure of ceria and the presence of oxygen vacancies. The presence of two different oxidation states Ce^{4+} and Ce^{3+} was inferred from the XPS results. Higher OSC and better CO oxidation activity was observed for the ceria–zirconia mixed oxide. Incorporation of zirconia into the ceria lattice and formation of higher defective sites might be responsible for the better activity observed for the ceria–zirconia mixed oxide. The microwave induced solution combustion synthesis method could be employed profitable to make veracious ceria-based mixed oxides. This method characterized by its simplicity, flexibility, and the easy control of different experimental factors.

Acknowledgements GKR thank UGC, New Delhi for senior research fellowship. The support of CICECO is also acknowledged.

References

1. Rao CNR (1994) Chemical approaches to the synthesis of inorganic materials. Wiley Eastern Limited, New Delhi
2. Fraigi LB, Lamas DG, de Reca NEW (2001) Mater Lett 47:2001
3. Bhaduri S, Bhaduri SB, Zhou E (1998) J Mater Res 13:156
4. Bhaduri S, Bhaduri SB, Prisbery KA (1999) J Mater Res 14:3571
5. Venkatachari KR, Huang D, Ostrander SP, Schulze WA, Stangle GC (1995) J Mater Res 10:748
6. Schafer J, Sigmund W, Roy S, Aldinger F (1997) J Mater Res 12:2518
7. Garcia R, Hirata GA, Mckittrick J (2001) J Mater Res 16:1059
8. Roy S, Sigmund W, Aldinger F (1999) J Mater Res 14:1524
9. Yong-hua L, Rong L, Yi-Yi L (2001) J Alloys Compd 319:108
10. Li L, Saita I, Saito K, Akiyama T (2002) Intermetallics 10:927
11. Greca MC, Moraes C, Segadaes AM (2001) Appl Catal A Gen 216:267
12. Civera A, Pavese M, Saracco G, Specchia V (2003) Catal Today 83:199
13. Vasylkiv O, Sakka Y, Skorokhod VV (2007) J Eur Ceram Soc 27:585

14. Vasylkiv O, Sakka Y (2005) Nano Lett 5:2598
15. Mingos DMP, Whittaker AG (1996) In: van Eldik R, Hubbard CD (eds) Chemistry under extreme or non-classical conditions. Wiley, New York, p 479
16. Shao Z, Halle SA (2004) Nature 431:170
17. Laosiripojana N, Assabumrungrat S (2005) Appl Catal B Envi 60:107
18. Kharton VV, Kovalevsky AV, Viskup AP, Shaula AL, Figueiredo FM, Naumovich EN, Marques FMB (2003) Solid State Ionics 160:247
19. Levy C, Guizard C, Julbe A (2004) Sep Purif Technol 32:327
20. Yin X, Hong L, Liu Z-L (2006) Appl Catal A Gen 300:75
21. Damyanova S, Bueno JMC (2003) Appl Catal A Gen 253:135
22. Ozaki T, Masui T, Machida K-I, Adachi G-Y, Sakata T, Mori H (2000) Chem Mater 12:643
23. Aneggi E, de Leitenburg C, Dolcetti G, Trovarelli A (2006) Catal Today 114:40
24. Mishra VS, Mahajani VV, Joshi JB (1995) Ind Eng Chem Res 34:2
25. Zafiris GS, Gorte RJ (1993) J Catal 139:561
26. Jacobs G, Khalid S, Patterson PM, Sparks DE, Davis BH (2004) Appl Catal A Gen 268:255
27. Montoya JA, Romero E, Gimon C, Del Angel P, Monzon A (2000) Catal Today 63:71
28. Craciun R, Daniell W, Knozinger H (2002) Appl Catal A Gen 230:153
29. Kawi S, Tang YP, Hidajat K, Yu LE (2005) J Metastable Nanocryst Mater 23:95
30. Neylon MK, Castagnola MJ, Castagnola NB, Marshall ChL (2004) Catal Today 96:53
31. Klug HP, Alexander LE (1974) X-ray diffraction procedures for polycrystalline and amorphous materials, 2nd edn. Wiley, New York
32. Briggs D, Seah MP (1990) Practical surface analysis: Auger and X-ray photoelectron spectroscopy, vol 1, 2nd edn. Wiley, New York
33. Wagner CD, Riggs WM, Davis LE, Moulder JF (1978) In: Muilenberg GE (ed) Handbook of X-ray photoelectron spectroscopy. Perkin-Elmer Corporation, Eden Prairie, MN
34. Chen Q, Shi Y, Chen J, Shi J (2005) J Mater Res 20:1409
35. Fagherazzi G, Polizzi S, Bettinelli M, Speghini A (2000) J Mater Res 15:586
36. Fumo DA, Morelli MR, Segadaes AM (1996) Mater Res Bull 31:1243
37. Purohit RD, Sharma BP, Pillai KT, Tyagi AK (2001) Mater Res Bull 36:2711
38. Patil KC, Aruna ST, Ekambaram S (1997) Curr Opin Solid State Mater Sci 2:158
39. Chick LA, Pederson LR, Maupin GD, Bates JL, Thomas LE, Exarhos GJ (1990) Mater Lett 10:6
40. Reddy BM, Reddy GK, Khan A, Ganesh I (2007) J Mater Sci 42:3557. doi:10.1007/s10853-007-1560-7
41. Reddy BM, Khan A, Yamada Y, Kobayashi T, Loridant S, Volta JC (2003) J Phys Chem B 107:5162
42. Preuss A, Gruehn R (1994) J Solid State Chem 110:363
43. Dutta G, Waghmare UV, Baidya T, Hegde MS, Priolkar KR, Sarode PR (2006) Chem Mater 18:3249
44. Reddy BM, Khan A, Yamada Y, Kobayashi T, Loridant S, Volta JC (2003) Langmuir 19:3025
45. Reddy BM, Lakshmanan P, Bharali P, Saikia P, Thrimurthulu G, Muhler M, Grunert W (2007) J Phys Chem C 111:10478
46. Martinez-Arias A, Fernandez-Garcia M, Salamanca LN, Valenzuela RX, Conesa JC, Soria J (2000) J Phys Chem B 104:4038
47. Shyu JZ, Weber WH, Gandhi HS (1988) J Phys Chem 92:4964
48. Lin X-M, Li L-P, Li G-S, Su W-H (2001) Mater Chem Phys 69:236
49. Reddy BM, Khan A, Yamada Y, Kobayashi T, Loridant S, Volta JC (2002) J Phys Chem B 106:10964
50. Spanier JE, Robinson RD, Zhang F, Chan S-W, Herman IP (2001) Phys ReV B 64:245407
51. Weber WH, Hass KC, McBride JR (1993) Phys Rev B 48:178
52. McBride JR, Hass KC, Poindexter BD, Weber WH (1994) J Appl Phys 76:2435
53. Wachs IE, Deo G (1991) J Phys Chem 95:5889
54. Yashima M, Arashi H, Kakihana M, Yoshimura M (1994) J Am Ceram Soc 77:1067
55. Weckhuysen BM, Schoonheydt RA (1999) Catal Today 49:441
56. Reddy BM, Bharali P, Saikia P, Park S-E, van den Berg MWE, Muhler M, Grunert W (2008) J Phys Chem C 112:11729
57. Escribano VS, Lopez EF, Panizza M, Resini C, Amores JMG, Busca G (2003) Solid State Sci 5:1369
58. Rango R, Kaspar G, Meriani S, di Monte R, Graziani M (1994) Catal Lett 24:107
59. Burroughs P, Hamnett A, Orchard A, Thornton G (1976) J Chem Soc Dalton Trans 1686
60. Pfau A, Schierbaum KD (1994) Surf Sci 321:71
61. Barr TL, Fries CE, Cariati F, Bart JCJ, Giordano N (1983) J Chem Soc Dalton Trans 1825
62. Bensalem A, Bozon-Verduraz F, Delamar M, Bugli G (1995) Appl Catal A Gen 121:81
63. Noronha FB, Fendley EC, Soares RR, Alvarez WE, Resasco DE (2001) Chem Eng J 82:21
64. Biener J, Baumer M, Wang J, Madrix R (2000) J Surf Sci 450:12
65. Galtayries A, Sporken R, Riga J, Blanchard G, Caudano R (1998) J Electron Spectrosc Relat Phenom 88–91:951
66. Reddy BM, Chowdhury B, Reddy EP, Fernandez A (2001) Appl Catal A Gen 213:279
67. Wang S-P, Zheng X-C, Wang X-Y, Wang X-R, Zhang S-M, Yu L-H, Huang W-P, Wu S-H (2005) Catal Lett 105:163
68. Reddy BM, Lakshmanan P, Loridant S, Yamada Y, Kobayashi T, Cartes CL, Rojas TC, Fernandez A (2006) J Phys Chem B 110:9140
69. Reddy BM, Rao KN, Reddy GK, Khan A, Park S-E (2007) J Phys Chem B 111:18751
70. Ozawa M, Loong CK (1999) Catal Today 50:329
71. Reddy BM, Saikia P, Bharali P, Yamada Y, Kobayashi T, Muhler M, Grunert W (2008) J Phys Chem C 112:16393
72. Reddy BM, Bharali P, Saikia P (2008) Catal Surv Asia 12:214
73. Boaro M, Vicario M, de Leitenburg C, Dolcetti G, Trovarelli A (2003) Catal Today 77:407